Short Communication

Investigating the deformation and microstructural evolution of laser powder-bed fusion of Hastelloy X during high temperature fatigue loading

Reza Esmaeilizadeh [a,b], Xiaolong Li [c], Mathias Kuhlow [c], Stuart Holdsworth [c], Ali Keshavarzkermani [a], Hamid Jahed [b], Ehsan Toyserkani [a], Ehsan Hosseini [c,*]

[a] *Multi-Scale Additive Manufacturing Laboratory (MSAM), University of Waterloo, 200 University Avenue West, Waterloo, ON N2L3G1, Canada*
[b] *Fatigue and Stress Analysis Laboratory (FATSLab), Department of Mechanical & Mechatronics Engineering, University of Waterloo, 200 University Avenue West, Waterloo, ON N2L 3G1, Canada*
[c] *Empa, Swiss Federal Laboratories for Material Science and Technology, Überlandstrasse129, Dübendorf CH-8600, Switzerland*

ARTICLE INFO

ABSTRACT

This study investigates the fatigue behaviour of samples made by laser powder-bed fusion of Hastelloy X (LPBF-HX) with as-built and machined surface conditions at 700 °C under fully reversed strain-controlled cyclic loading. Samples with both surface conditions exhibited initially cyclic hardening followed by cyclic softening under large strain amplitude testing, where a slight continuous hardening was observed for tests with smaller strain amplitudes. The samples with machined surfaces showed longer endurance and higher stress ranges than those with as-built surfaces. Post-fatigue-test EBSD analysis showed the formation of the Goss texture and extensive local strain accumulation in the samples tested under high strain amplitude at 700 °C. Fractography investigations revealed that early crack initiation in the samples with as-built surfaces was from stress concentrations induced by valleys on the rough surface. No evidence of crack initiation induced by pre-existing defects was observed in the machined samples, and the excessive slip activity at the surface was found to be responsible for the crack initiation.

1. Introduction

Additive manufacturing (AM) has revolutionized the production of complex parts by building them layer-by-layer [1,2]. Laser powder-bed fusion (L-PBF), a leading AM technology, excels in creating high-resolution complex metallic parts due to its small laser spot size (~70–100 μm) [3]. The fast-moving small laser heat source in L-PBF results in high heating and cooling rates, leading to a fine cellular solidification structure, epitaxial grain growth, and significant residual stresses. Consequently, L-PBF materials possess distinct mechanical properties compared to those produced conventionally [4,5], necessitating thorough characterization to fully understand the behavior of L-PBF builds [6–8].

Hastelloy X (HX), a solid solution-strengthened nickel-based superalloy, is known for its high strength and oxidation resistance at elevated temperatures [9,10], making it suitable for gas turbine engines and petrochemical reactors. Its excellent weldability, due to low Ti + Al content, makes it ideal for producing complex parts through AM [8,9]. Several studies have examined the microstructure and static properties

of AM HX [10–15]. Although the application of LPBF-HX often involves cyclic loading at high temperatures, only limited studies [16–22] have been devoted to investigating its fatigue response, particularly at elevated temperatures.

The fatigue life of AM alloys is influenced by factors like strength, ductility [16], defect state [17], and surface roughness [18,19]. Our prior work on LPBF-HX at room temperature (RT) identified static strength as crucial in the low cycle fatigue regime, with defects and surface roughness impacting the high cycle fatigue regime [20]. Han et al. [21] observed improved RT fatigue performance in machined and HIPed samples due to defect removal and residual stress reduction. Montero-Sistiaga et al. [22] found inconsistent fatigue lives in their LPBF-HX samples, attributed to presence of lack-of-fusion defects. Few studies have addressed LPBF-HX high-temperature (HT) fatigue response. Examples include Saarimäki et al. [23], who examined LPBF-HX crack growth during dwell-fatigue tests at 700 °C, and Lei et al. [24], who reported a reduction in fatigue performance of the alloy by increasing test temperatures from 400 °C to 600 °C.

This study systematically investigates the high-temperature cyclic

---

deformation and failure response of LPBF-HX, comparing it with previous findings on fatigue loading at room temperature. It assesses cyclic stress and strain responses and conducts post-test microstructural analyses to understand the deformation and failure response of LPBF-HX under high-temperature fatigue loading. Given that the geometrical complexity of LPBF parts often precludes surface finishing, this research also investigates the impact of as-built surface roughness on hysteresis loops, fatigue endurance, and crack initiation and growth response.

2. Methods and materials

2.1. Specimen fabrication

An EOS M290 printer was used to produce specimens using commercially available HX powder from EOS GmbH, with a particle size of 15–45 μm. The specimens were fabricated under an argon atmosphere with a build plate temperature of 80 °C. To achieve >99.98 % relative density, a set of optimum process parameters including laser power of 195 W, laser scanning speed of 850 mm/s, hatching distance of 90 μm, and a layer thickness of 40 μm were used, without any skin scans, based on the authors' previous studies [20,25,26]. A scanning vector rotation of 67° was used between successive layers, and all samples were printed vertically, such that the loading direction during mechanical testing was parallel to the building direction. Net shape samples were printed according to the drawing presented in Fig. 1a, with M7 threads machined at the ends before mechanical testing. Cylinders were also printed for later machining and mechanical testing of the surface-machined LPBF-HX (Fig. 1b). Henceforth, machined samples and net shape samples tested at high temperature (HT) will be referred to as HT-Machined (HT-M) and HT-As-Built (HT-AB) samples, respectively. No post-process heat treatment was applied to the test pieces before fatigue tests. This implies the existence of some levels of residual stress in both sample categories, although being moderated by relaxation during heating up ramps and stabilization period at 700 °C before the start of fatigue loading.

2.2. Mechanical testing

The study conducted twelve isothermal strain-controlled fatigue tests at 700 °C with a strain ratio of $R_\varepsilon = -1$ for both HT-M and HT-AB HX samples. A 100 kN servo-hydraulic MTS machine with an induction heating system (Fig. 1c) was used to conduct the tests at a strain rate of $0.2\%\text{s}^{-1}$. A class 0.5 side-entry extensometer with a datum leg spacing of 15 mm was used to measure strain, while the built-in load cell of the testing machine monitored force. During the fatigue tests, data on force (transformed to stress using nominal diameters) and strain were recorded at a frequency of 10 Hz, along with the peak/valley stress for each cycle. Three type-K thermocouples were attached along the specimen gauge length to measure temperature and maintain a temperature gradient of less than 3 °C. It is worth noting that the thermocouples were mechanically tied to the specimen surface and not spot-welded to avoid premature crack initiation at weld spots. Tests were conducted at strain amplitudes of 0.2 %, 0.4 %, and 0.8 % to allow comparison with previous examination results at room temperature [20]. Two repeat tests were performed for each condition, and the ISO 12,106 standard was followed for the testing procedure, where possible.

2.3. Microstructural and fracture surface characterization

The microstructure investigation involved the examination of cross-sections perpendicular to the print direction for LPBF-HX, both before and after fatigue testing. The standard metallography sample preparation procedure was followed, which included cutting, mounting, grinding with SiC grinding paper (ranging from 80 to 4000 grit), and final polishing using a 1–0.05 μm alumina slurry and colloidal silica suspension with vibratory polishing (Buehler VIBROMET 2). For the post-test evaluation, fatigue samples that underwent various strain amplitudes were examined, specifically focusing on cross-sections approximately 2 mm below the fracture surface. A JEOL7000F scanning electron microscope (SEM) equipped with an Oxford EBSD detector was utilized to investigate grain orientations and crystallographic texture. The EBSD data collection and post-processing were performed using AZtecHKL and HKL Channel 5 software. Furthermore, the fracture surfaces of the samples following fatigue testing were analyzed using a TESCAN VEGA3 scanning electron microscope (SEM). This analysis aimed to identify crack initiation sites and gain insight into the crack growth response of the samples.

3. Results and discussions

3.1. Mechanical response

While the supplementary materials provide all the data from the conducted mechanical tests, examples of the recorded data are presented and discussed below. Fig. 2a and b illustrate the evolution of hysteresis loops derived from repeat tests performed on HT-AB and HT-
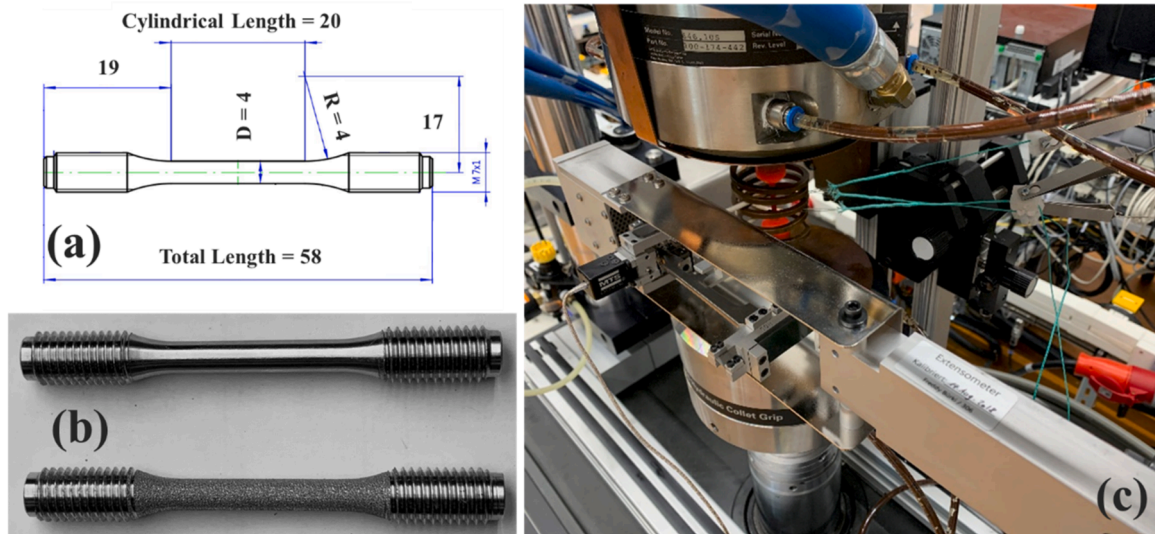

Fig. 1. (a) Specimen drawing for mechanical testing (dimensions in mm), (b) Samples with as-built and machined surfaces, (c) Employed mechanical testing setup.
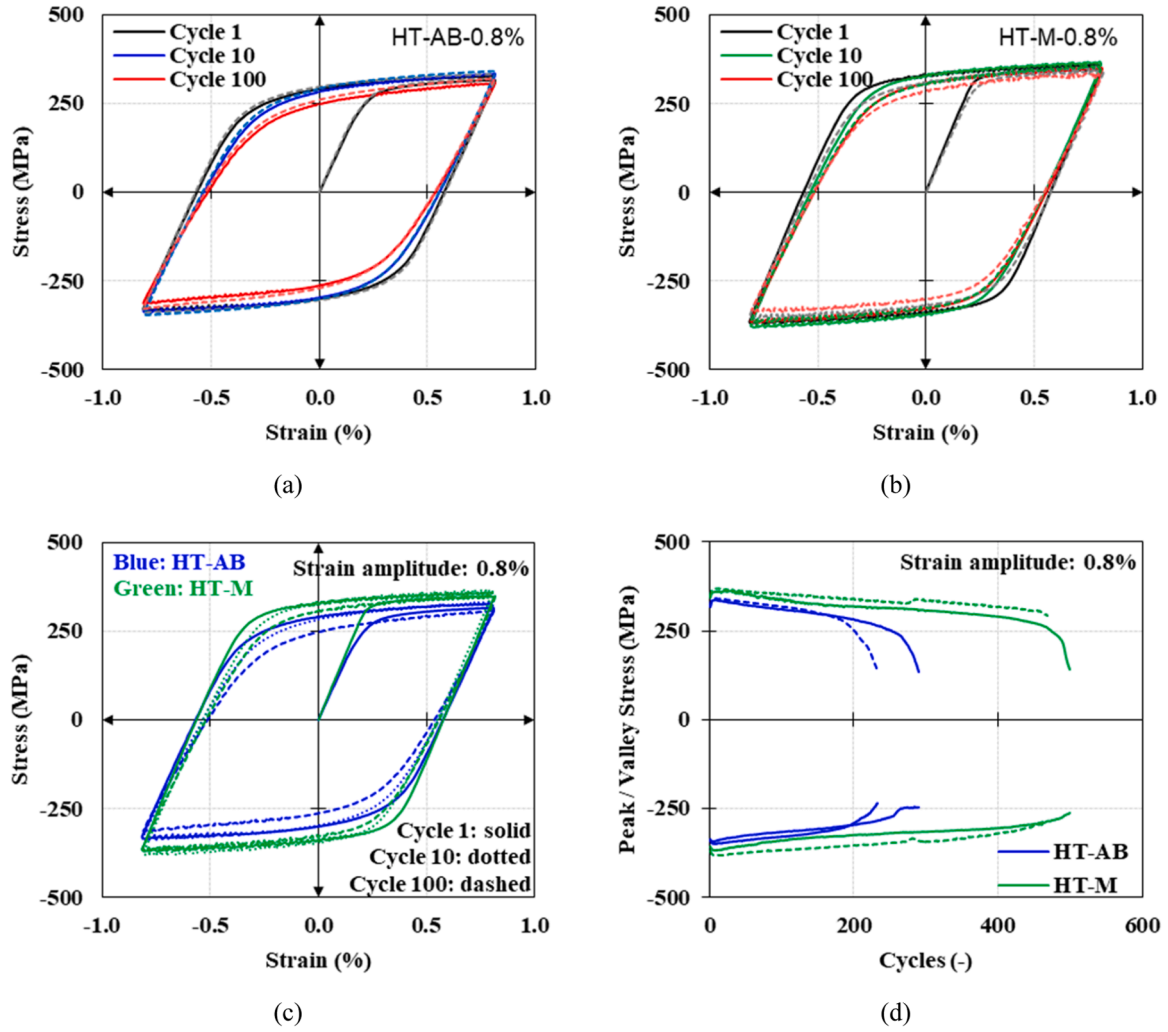
Fig. 2. (a) Presentation of hysteresis loops for HT-AB HX at cycles 1, 10, and 100 from two repeat tests at 700 °C. (b) Presentation of hysteresis loops for HT-M HX at cycles 1, 10, and 100 from two repeat tests at 700 °C. (c) Comparison of hysteresis loops between HT-AB and HT-M HX at cycles 1, 10, and 100. (d) Evolution of peak/valley stresses for HT-AB and HT-M HX from two repeat tests at 700 °C (all presented data are from tests with a strain amplitude of 0.8 % and the solid lines are for the first tests and the dashed lines are for the repeat/second tests).

M HX with a strain amplitude of 0.8 %. Additionally, Fig. 2c and d compare the hysteresis loops and the evolution of peak-valley stresses for HT-AB and HT-M HX under the same strain amplitude.

A comparison of the hysteresis loops between the repeated tests demonstrates a generally repeatable deformation response in the samples, particularly in the first cycle. Observations from Fig. 2d, however, indicate some variability in the fatigue endurance response of LPBF-HX, particularly for the samples with as-built surfaces, which are believed to arise from the high sensitivity of fatigue crack initiation life to the variability in the state of defects at the surface, i.e. roughness.

Comparing the hysteresis and peak/valley stress response of HT-AB and HT-M HX from Figs. 2c and d, respectively, it can be observed that the samples in the machined state exhibit a stronger response in terms of deformation and life compared to the samples with the as-built surface condition. The stronger deformation response can be attributed to the adoption of the same nominal cross-section for stress calculation for both sample categories, although the actual load-carrying cross-section for AB samples is smaller due to the high surface roughness. Similarly, the shorter endurance of AB samples is attributed to their surface roughness, which facilitates fatigue crack initiation from the surface [20,27–29].

It should be noted that indications of serrated stress-strain response were observed in both tension-reversal and compression-reversal

loadings for the samples, particularly for larger cycle numbers. These serrations are related to the interaction of mobile dislocations with solute atoms, known as the dynamic strain aging (DSA) phenomenon. These observations align with recent evidence reported in [14], indicating that although extensive DSA occurs for LPBF HX in the temperature range of 300–600 °C, it is limited to relatively high strain rates and only after the accumulation of a large amount of plastic strain at 700 °C. Furthermore, it should be mentioned that the observed hysteresis loops appear to be symmetric, indicating that slip is the dominant plastic deformation mechanism at the examined temperatures [29].

Fig. 3a presents a comparison of the stress ranges observed during cyclic loading of HT-AB and HT-M HX samples under various strain amplitudes. At larger strain amplitudes and for both surface conditions, an initial cyclic hardening phase is observed, characterized by an increase in stress range during the early cycles. This is followed by a subsequent steady-state period with a gradual decrease in stress range (cyclic softening) and, finally crack initiation and failure. Conversely, minimal cyclic hardening is observed for samples tested at the lowest strain amplitude, as the deformation mainly remains in the elastic regime during cycles. These findings align with those reported for LPBF-HX at room temperature [25], but differ significantly from those reported for conventionally manufactured HX at elevated temperatures [30], where a pronounced cyclic hardening was observed across various
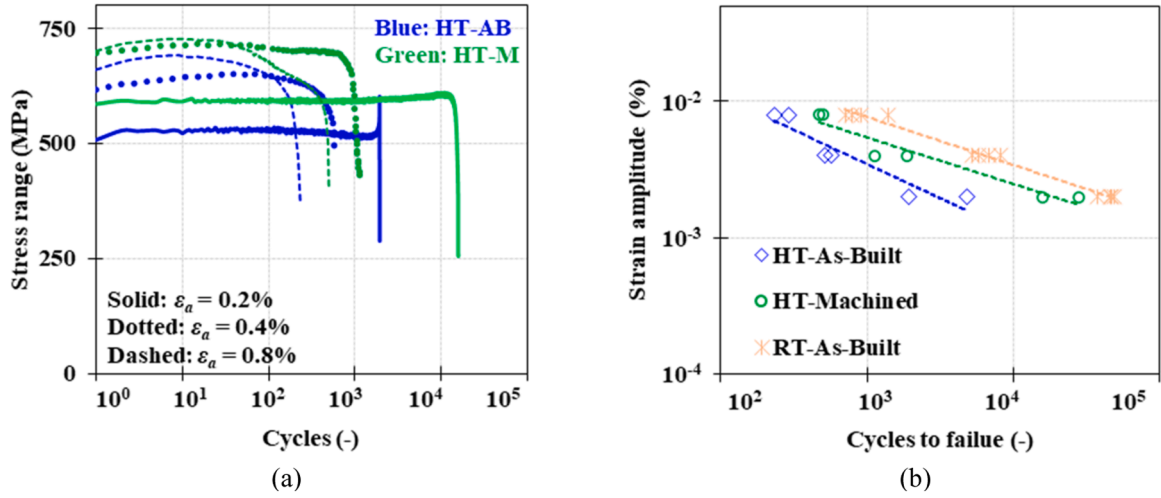
Fig. 3. (a) Evolution of peak/valley stresses for HT-AB and HT-M HX from tests with various strain amplitudes, showing the primary cyclic hardening followed by cyclic softening. (b) Cycles to failure as a function of strain amplitude for HT-AB and HT-M HX, as well as for RT-AB HX.

strain amplitudes. This difference can be attributed to the significantly higher dislocation density in the LPBF alloy [14], which restricts hardening during subsequent (cyclic) deformation.

In Fig. 3b, the dependence of failure endurance on strain amplitude is compared between HT-AB and HT-M HX. As expected, samples exhibit increased fatigue life by decreasing the strain amplitude, indicating reduced damage associated with each cycle at lower strain amplitudes. Consistent with previous studies investigating the influence of surface roughness on fatigue endurance [27,28,31–33], machined LPBF-HX samples demonstrate longer fatigue lives than samples with as-built surface states, particularly at lower strain amplitudes. Plastic deformation and dislocation slip are the dominant fatigue crack initiation mechanisms at higher strain amplitudes, and surface roughness has a marginal effect. Conversely, at lower strain amplitudes where cyclic deformation is predominantly elastic, surface defects are the dominant site for fatigue crack initiation, and therefore increased surface roughness significantly decreases fatigue strength.

It should be highlighted that the crack initiation in the HT-AB sample, tested at a 0.2 % strain amplitude, occurred within the testpiece parallel length but outside the extensometer gauge length. Because the testing machine controls the applied strain range based on extensometer readings, crack initiation outside this gauge length results in the observed increase in stress range post-crack initiation, as depicted in

Fig. 3a. While this does not affect the crack initiation endurance, it is expected to accelerate crack growth, thereby potentially affecting the failure endurance.

Fig. 4a presents a comparison of the observed mid-life hysteresis response of AB HX at elevated temperature, obtained from tests with strain amplitudes of 0.8 % and 0.4 %, with the response at room temperature reported in our previous study [25]. Both the elevated temperature and room temperature tests exhibit symmetric hysteresis loops; however indications of DSA were found only in the high-temperature tests. The hysteresis loops obtained at 700 °C exhibit a wider width at zero stress level compared to those at room temperature, indicating a higher degree of plastic strain accumulation during cyclic loading. Consequently, the plastic damage associated with each cycle at high temperatures is higher compared to the same strain amplitudes at room temperature, resulting in shorter fatigue life, as shown in Fig. 3b.

Fig. 4b illustrates the evolution of the stress range during cyclic loading of AB-HX at room and elevated temperature under strain amplitudes of 0.8 % and 0.4 %. Notably, the samples tested at room temperature exhibit more significant cyclic hardening over a larger number of cycles, whereas only a slight hardening is observed for the samples tested at high temperatures. These findings can be attributed to the higher activity of recovery and softening mechanisms at elevated temperatures. However, a detailed examination of the hardening/softening
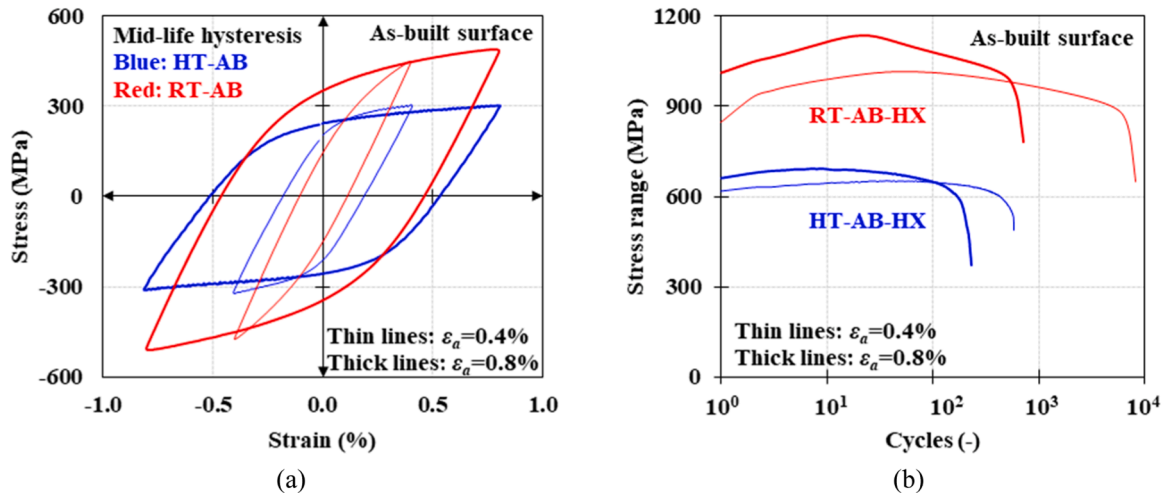

Fig. 4. (a) Comparison of mid-life hysteresis loops for AB HX at room temperature (RT) and 700 °C (HT) for tests with strain amplitudes of 0.8 % and 0.4 %. (b) Evolution of peak/valley stresses for HT-AB and RT-AB HX from tests with strain amplitudes of 0.8 % and 0.4 %.

mechanisms at different temperatures requires more in-depth analysis and is beyond the scope of this study.

3.2. Microstructural investigations

Fig. 5 presents the results of EBSD microscopy examination for LPBF HX in its as-built state and after fatigue testing under strain amplitudes of 0.2 % and 0.8 % for HT-AB, HT-M, and RT-AB samples. The Inverse pole figure (IPF-Z) map of the as-built sample shows no indication of any specific texture. The kernel average misorientation map of this sample indicates a high density of geometrically necessary dislocations (GND), which is typical for LPBF samples, and is also reported in [34–36].

For both strain amplitudes tested at room temperature, no significant differences are observed in the grain structure and orientation compared to the as-built microstructure. When comparing the microstructure of the sample loaded at room temperature under 0.2 % and 0.8 % strain amplitudes, the latter exhibits greater local misorientation, indicating higher strain localization. This strain localization leads to accelerated crack initiation, i.e. in line with the observed shorter fatigue life for larger strain amplitudes.

Similar to the samples tested at room temperature, the grain morphology of the samples after cyclic loading at 700 °C remains unchanged compared to the as-built state, and there is no indication of recrystallization during fatigue loading. A closer examination of the KAM maps reveals a significantly higher density of GND in the HT-M sample loaded under a strain amplitude of 0.8 %. This higher density could be attributed to a larger amount of plastic strain accumulation over the 500 cycles in this particular sample compared to the others.

Interestingly, in contrast to the observations for samples tested at room temperature, the pole figures of the samples tested at 700 °C show a strong realignment of grains and the formation of Goss texture (<110>//LD) during fatigue loading. Previous studies have reported the formation of a <111>//LD texture during monotonic loading at both room temperature and 700 °C [10,37,38]. This texture formation can be explained by the slip of dislocations through {111}<112> slip systems in FCC materials, aligning the ⟨100⟩ and ⟨111⟩ orientations with the loading direction [38,39].

However, the current observations suggest the alignment of the ⟨110⟩ orientation along the loading direction during cyclic loading. Goss and rotated Goss textures are typically associated with dynamic recrystallization (DRX) in FCC alloys [40,41]. Some extent of DRX has been previously observed by the authors during low strain rate tensile testing at 700 °C for LPBF-HX [14]. However, the overall high KAM values in the samples after fatigue testing (Fig. 5b) do not confirm the

occurrence of DRX during the conducted fatigue tests. Further investigation is therefore necessary to understand the mechanisms responsible for the formation of Goss textures during high-temperature cyclic deformation of LPBF-HX.

3.3. Fracture surface

Fig. 6 presents representative examples of the fracture surfaces of the HT-AB-0.4 % and HT-M-0.4 % samples, where similar observations were made for the other samples. The figure highlights different stages of fatigue crack development using distinct colours: green, blue, and red representing crack initiation, propagation, and final fracture, respectively.

Interestingly, fatigue cracks were observed to initiate from multiple sites on the surface of both AB and M samples. This is noteworthy as previous reports [17,42,43] have often attributed fatigue crack initiation in machined LPBF samples to internal gas pores or lack of fusion defects. However, in this study, optimized process parameters resulted in nearly fully dense builds, eliminating initiation from defects in the bulk/center of the sample. For samples with an as-built surface condition, stress concentrations at the valleys of the rough surface act as the primary fatigue crack initiation sites (Fig. 6a inset) and tear ridges, similar to previous reports [27,28,44].

The crack initiation sites for machined samples are located near the surface, and the presence of semi-elliptical tear ridges at these sites indicates excessive slip activity as the primary mechanism for crack initiation [45,46]. Therefore, this crack initiation mechanism necessitates a significant amount of cyclic loading to accumulate sufficient strain at these sites, particularly at lower strain amplitudes.

In the stable fatigue crack growth region (blue area in Fig. 6), the presence of striations indicates incremental advancement of the crack with each cycle. A striation spacing of approximately 3.5 μm was observed at a crack length of approximately 1–1.25 mm for samples with both machined and as-built surfaces, suggesting a similar crack growth rate irrespective of the surface condition. Ultimately, when the crack length reaches its critical value, final failure occurs, which is characterized by the presence of dimples in the final fracture region for samples with both surface conditions (red area in Fig. 6).

Fatigue life primarily consists of the time taken for fatigue crack initiation and the duration of stable fatigue crack propagation until final fracture. The similar spacing of striations in samples with both machined and as-built surface conditions indicates an equal crack growth rate. Considering the comparable size of the stable crack growth region for samples with different surface conditions (Fig. 6), crack growth kinetics
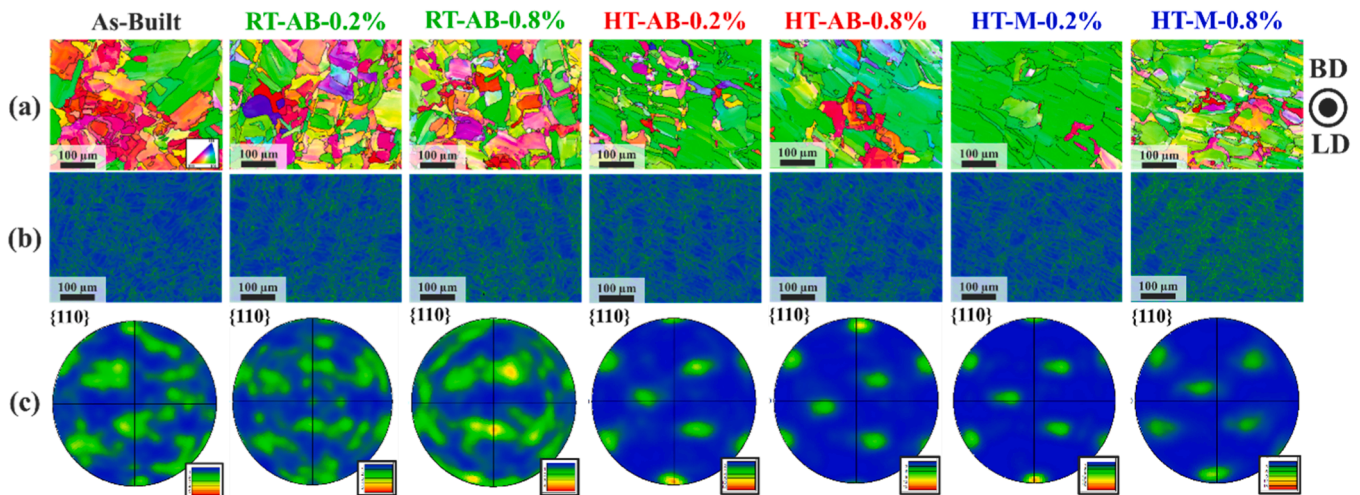

Fig. 5. (a) EBSD IPF-Z maps, (b) Kernel average misorientation (KAM) maps and (c) {110} pole figures for LPBF HX in its as-built state and after fatigue testing (approximately 2 mm below the fracture surface) under strain amplitudes of 0.2 % and 0.8 % for HT-AB, HT-M, and RT-AB samples.
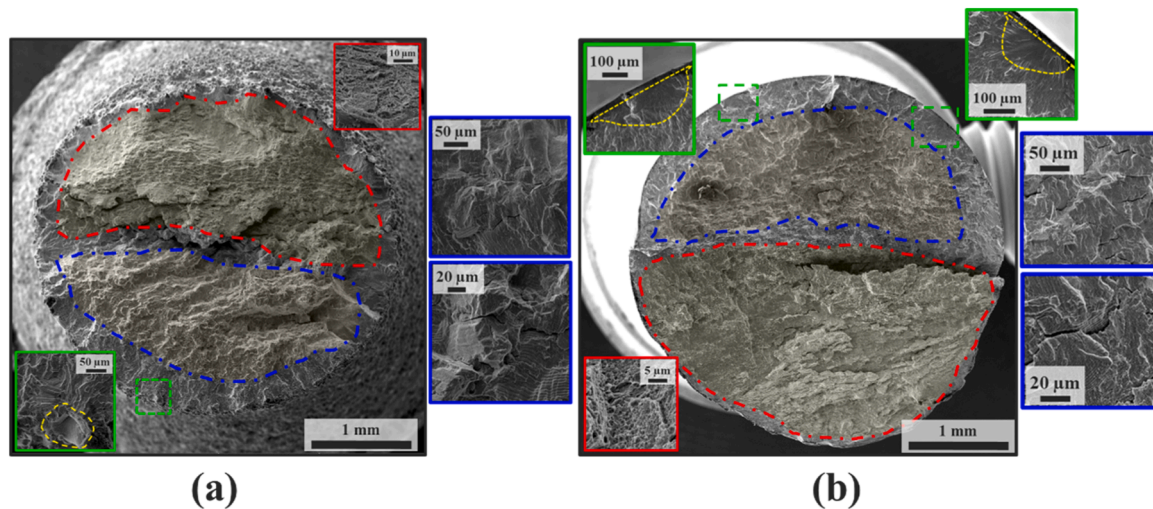
Fig. 6. Examples of fracture surfaces of fatigue-loaded LPF-HX samples illustrating different stages of crack development: crack initiation (green), crack propagation (blue), and final fracture (red). (a) HT-AB-0.4 % and (b) HT-M-0.4 %.

cannot explain the longer fatigue lives observed in the machined samples. Therefore, the difference in fatigue lives should be attributed to the crack initiation stage. In the as-built samples, the surface valleys serve as pre-existing crack initiation sites, significantly reducing the required number of cycles for crack initiation. On the other hand, machined surface samples require a substantial amount of loading cycles to generate sufficient slip activity and initiate cracks, resulting in longer fatigue endurance.

4. Conclusions

This study investigated the cyclic deformation and fatigue life response of LPBF HX at 700 °C under different strain amplitudes, considering samples with both machined and as-built surfaces. The mechanical experiments were complemented by EBSD and fracture surface analyses, and the findings were compared to previous studies on the fatigue behaviour of the alloy at room temperature. The following conclusions have been drawn:

(1) The fatigue experiments at 700 °C revealed a range of cyclic hardening/softening behaviour. High strain amplitude tests exhibited initial cyclic hardening followed by cyclic softening, while the lowest strain amplitude tests showed only slight hardening.

(2) EBSD analysis revealed substantial local strain accumulation in samples subjected to high strain amplitudes at both room and high temperatures. While cyclic loading at room temperature did not result in significant changes in grain orientation, the fatigue loading at 700 °C led to grain orientation alignment and formation of the Goss texture.

(3) Samples with the as-built surface condition exhibited an inferior fatigue life response compared to the machined samples. Fractography investigations revealed that fatigue cracks initiated from multiple sites on the surface of samples with both as-built and machined surfaces. In the case of as-built surfaces, fatigue cracks initiated early from the valleys of surface roughness, whereas semi-elliptical crack initiation morphologies observed in machined samples indicated crack initiation due to excessive slip activity, thus requiring substantial cyclic loading.

CRediT authorship contribution statement

Reza Esmaeilizadeh: Writing – review & editing, Writing – original

draft, Methodology, Investigation. **Xiaolong Li:** Writing – review & editing, Methodology, Investigation. **Mathias Kuhlow:** Investigation. **Stuart Holdsworth:** . **Ali Keshavarzkermani:** Writing – review & editing, Investigation. **Hamid Jahed:** Writing – review & editing, Investigation. **Ehsan Toyserkani:** Writing – review & editing, Investigation. **Ehsan Hosseini:** Writing – review & editing, Writing – original draft, Project administration, Methodology, Investigation.

Declaration of competing interest

The authors declare that they have no known competing financial interests or personal relationships that could have appeared to influence the work reported in the article titled:

Data availability

Data will be made available on request.

Supplementary materials

Supplementary material associated with this article can be found, in the online version, at doi:10.1016/j.addlet.2024.100201.

References

[1] E. Toyserkani, D. Sarker, O.O. Ibhadode, F. Liravi, P. Russo, K. Taherkhani. Metal Additive Manufacturing, John Wiley & Sons Ltd, Hoboken, New Jersey, USA, 2021.

[2] E. Davoodi, H. Montazerian, A.S. Mirhakimi, M. Zhianmanesh, O. Ibhadode, S. I. Shahabad, R. Esmaeilizadeh, E. Sarikhani, S. Toorandaz, S.A. Sarabi, R. Nasiri, Y. Zhu, J. Kadkhodapour, B. Li, A. Khademhosseini, E. Toyserkani, Additively manufactured metallic biomaterials, Bioact. Mater. 15 (2022) 214–249.

[3] H. Fayazfar, M. Salarian, A. Rogalsky, D. Sarker, P. Russo, V. Paserin, E. Toyserkani, A critical review of powder-based additive manufacturing of ferrous alloys: process parameters, microstructure and mechanical properties, Mater. Des. 144 (2018) 98–128.

[4] E. Hosseini, V.A. Popovich, A review of mechanical properties of additively manufactured Inconel 718, Addit. Manuf. 30 (2019) 100877.

[5] R. Esmaeilizadeh, U. Ali, A. Keshavarzkermani, Y. Mahmoodkhani, E. Marzbanrad, E. Toyserkani, On the effect of spatter particles distribution on the quality of Hastelloy X parts made by laser powder-bed fusion additive manufacturing, J. Manuf. Process. 37 (2019) 11–20.

[6] E. Sadeghi, P. Karimi, R. Esmaeilizadeh, F. Berto, S. Shao, J. Moverare, E. Toyserkani, N. Shamsaei, A state-of-the-art review on fatigue performance of powder bed fusion-built alloy 718, Prog. Mater. Sci. 133 (2023) 101066.

[7] U. Ali, R. Esmaeilizadeh, F. Ahmed, D. Sarker, W. Muhammad, A. Keshavarzkermani, Y. Mahmoodkhani, E. Marzbanrad, E. Toyserkani, Identification and characterization of spatter particles and their effect on surface roughness, density and mechanical response of 17-4 PH stainless steel laser powder-bed fusion parts, Mater. Sci. Eng. A 756 (2019) 98–107.

[8] Y. Mahmoodkhani, U. Ali, S. Imani Shahabad, A.R. Kasinathan, R. Esmaeilizadeh, A. Keshavarzkermani, E. Marzbanrad, E. Toyserkani, On the measurement of effective powder layer thickness in laser powder-bed fusion additive manufacturing of metals, Prog. Addit. Manuf. 4 (2018) 109–116.

[9] Culling J.H. (1994). Heat and Corrosion Resistant Iron-Nickel-Chromium Alloy. U. S. Patent No. 5,310,522.

[10] C.H. Yu, R.L. Peng, T.L. Lee, V. Luzin, J.E. Lundgren, J. Moverare, Anisotropic behaviours of LPBF Hastelloy X under slow strain rate tensile testing at elevated temperature, Mater Sci Eng A 844 (2022) 143174.

[11] A. Keshavarzkermani, R. Esmaeilizadeh, U. Ali, P.D. Enrique, Y. Mahmoodkhani, N.Y. Zhou, A. Bonakdar, E. Toyserkani, Controlling mechanical properties of additively manufactured hastelloy X by altering solidification pattern during laser powder-bed fusion, Mater. Sci. Eng. A 762 (2019) 138081.

[12] A.N. Jinoop, V.A. Kumar, C.P. Paul, R. Ranjan, K.S. Bindra, Hot deformation behavior of Hastelloy-X preforms built using directed energy deposition based laser additive manufacturing, Mater. Lett. 270 (2020) 127737.

[13] R. Wróbel, et al., Microstructure formation in micron-scale thin-walled Hastelloy X samples fabricated with laser powder bed fusion, Prog. Addit. Manuf. (2023) 1–13.

[14] X. Li, R. Esmaeilizadeh, H. Jahed, E. Toysarkani, M. Pham, S. Holdsworth, E. Hosseini, Effects of temperature and strain rate on tensile properties and dynamic strain aging behaviour of LPBF Hastelloy X, Addit. Manuf. Lett. 4 (2023) 100105.

[15] Sun Y., Huang R., Ma R., Tan C., Wang Y., Xue L., Lin D.Y., Song X., & Zhao H.Y. (n. d.). Investigation of microstructure and failure mechanisms at room and elevated temperature of Hastelloy X produced by laser powder-bed fusion. https://doi.org/1 0.2139/ssrn.4461835.

[16] S. Leuders, T. Lieneke, S. Lammers, T. Tröster, T. Niendorf, On the fatigue properties of metals manufactured by selective laser melting - The role of ductility, J. Mater. Res. 29 (2014) 1911–1919.

[17] G. Kasperovich, J. Hausmann, Improvement of fatigue resistance and ductility of TiAl6V4 processed by selective laser melting, J. Mater. Process. Technol. 220 (2015) 202–214.

[18] P.D. Enrique, A. Keshavarzkermani, R. Esmaeilizadeh, S. Peterkin, H. Jahed, E. Toyserkani, N.Y. Zhou, Enhancing fatigue life of additive manufactured parts with electrospark deposition post-processing, Addit. Manuf. 36 (2020) 101526.

[19] S. Romano, P.D. Nezhadfar, N. Shamsaei, M. Seifi, S. Beretta, High cycle fatigue behavior and life prediction for additively manufactured 17-4 PH stainless steel: effect of sub-surface porosity and surface roughness, Theor. Appl. Fract. Mech. 106 (2020) 102477.

[20] R. Esmaeilizadeh, A. Keshavarzkermani, U. Ali, B. Behravesh, A. Bonakdar, H. Jahed, E. Toyserkani, On the effect of laser powder-bed fusion process parameters on quasi-static and fatigue behaviour of Hastelloy X: a microstructure/ defect interaction study, Addit. Manuf. 38 (2021) 101805.

[21] Q. Han, R. Mertens, M.L. Montero-Sistiaga, S. Yang, R. Setchi, K. Vanmeensel, B. Van Hooreweder, S.L. Evans, H. Fan, Laser powder bed fusion of Hastelloy X: effects of hot isostatic pressing and the hot cracking mechanism, Mater. Sci. Eng. A (2018).

[22] M.L. Montero-Sistiaga, N.M. Dhansay, L. Bautmans, S. Nardone, T.H. Becker, J. P. Kruth, K. Vanmeensel, Fatigue performance of micro-crack free Hastelloy X produced by selective laser melting (SLM), Eur. Conf. Struct. Integr. Addit. Manuf. Mater. (2019) 9–11.

[23] J. Saarimäki, M. Lundberg, H. Brodin, J.J. Moverare, Dwell-fatigue crack propagation in additive manufactured Hastelloy X, Mater. Sci. Eng. A 722 (2018) 30–36.

[24] L. Lei, B. Li, H. Wang, G. Huang, F. Xuan, High-temperature high-cycle fatigue performance and machine learning-based fatigue life prediction of additively manufactured Hastelloy X, Int. J. Fatigue (2024) 178.

[25] R. Esmaeilizadeh, A. Keshavarzkermani, S. Faghih, B. Behravesh, U. Ali, A. Bonakdar, H. Jahed, E. Toyserkani, Fatigue characterization and modeling of additively manufactured Hastelloy-X Superalloy, J. Mater. Eng. Perform. 31 (2022) 6234–6245.

[26] R. Esmaeilizadeh, A. Keshavarzkermani, U. Ali, Y. Mahmoodkhani, B. Behravesh, H. Jahed, A. Bonakdar, E. Toyserkani, Customizing mechanical properties of additively manufactured Hastelloy X parts by adjusting laser scanning speed, J. Alloy. Compd. 812 (2020) 152097.

[27] N. Sanaei, A. Fatemi, Analysis of the effect of surface roughness on fatigue performance of powder bed fusion additive manufactured metals, Theor. Appl. Fract. Mech. 108 (2020) 102638.

[28] W. Beard, et al., The influence of surface finish and build orientation on the low cycle fatigue behaviour of laser powder bed fused stainless steel 316L, Mater. Sci. Eng. A 864 (2023) 144593.

[29] S.M.H. Karparvarfard, S.K. Shaha, S.B. Behravesh, H. Jahed, B.W. Williams, Fatigue characteristics and modeling of cast and cast-forged ZK60 magnesium alloy, Int. J. Fatigue 118 (2019) 282–297.

[30] G.V.P. Reddy, P. Harini, R. Sandhya, K.B. Sankara, R.K. Paretkar, On dual-slope linear cyclic hardening of Hastelloy X, Mater. Sci. Eng. A 527 (2010) 3848–3851.

[31] S. Lee, J.W. Pegues, N. Shamsaei, Fatigue behavior and modeling for additive manufactured 304L stainless steel: the effect of surface roughness, Int. J. Fatigue 141 (2020) 105856.

[32] S.A. McKelvey, A. Fatemi, Surface finish effect on fatigue behavior of forged steel, Int. J. Fatigue 36 (2012) 130–145.

[33] M.R. Bayoumi, A.K. Abdellatif, Effect of surface finish on fatigue strength, Eng. Fract. Mech. 51 (5) (1995) 861–870.

[34] S. Pourbabak, M.L. Montero-Sistiaga, D. Schryvers, J. Van Humbeeck, K. Vanmeensel, Microscopic investigation of as built and hot isostatic pressed Hastelloy X processed by selective laser melting, Mater. Charact. 153 (2019) 366–371.

[35] C.H. Yu, S. Jiang, X. Sun, R.L. Peng, J.E. Lundgren, J. Moverare, A new approach for determining GND and SSD densities based on indentation size effect: an application to additive-manufactured Hastelloy X, J. Mater. Sci. Technol. 96 (2022) 295–307.

[36] A. Keshavarzkermani, R. Esmaeilizadeh, P.D. Enrique, H. Asgari, N.Y. Zhou, A. Bonakdar, E. Toyserkani, Materials Characterization Static recrystallization impact on grain structure and mechanical properties of heat-treated Hastelloy X produced via laser powder-bed fusion, Mater. Charact. 173 (2021) 110969.

[37] C.H. Yu, R.L. Peng, V. Luzin, M. Sprengel, M. Calmunger, J.E. Lundgren, H. Brodin, A. Kromm, J. Moverare, Thin-wall effects and anisotropic deformation mechanisms of an additively manufactured Ni-based superalloy, Addit. Manuf. 36 (2020) 101672.

[38] O. Sanchez-Mata, X. Wang, J.A. Muñiz-Lerma, S.E. Atabay, M.A. Shandiz, M. Brochu, Characterization of the microstructure and mechanical properties of highly textured and single crystal Hastelloy X thin struts fabricated by laser powder bed fusion, J. Alloy. Compd. 901 (2022) 163465.

[39] M.G. Ardakani, M. McLean, B.A. Shollock, Twin formation during creep in single crystals of nickel-based superalloys, Acta Mater. 47 (1999) 2593–2602.

[40] K. Tazuddin Biswas, N.P. Gurao, Deciphering micro-mechanisms of plastic deformation in a novel single phase fcc-based MnFeCoNiCu high entropy alloy using crystallographic texture, Mater. Sci. Eng. A 657 (2016) 224–233.

[41] M. Wang, C. Sun, M.W. Fu, Z. Liu, C. Wang, Microstructure and microtexture evolution of dynamic recrystallization during hot deformation of a nickel-based superalloy, Mater. Des. 188 (2020) 108429.

[42] P. Edwards, M. Ramulu, Fatigue performance evaluation of selective laser melted Ti-6Al-4V, Mater. Sci. Eng. A 598 (2014) 327–337.

[43] S. Leuders, M. Thöne, A. Riemer, T. Niendorf, T. Tröster, H.A. Richard, H.J. Maier, On the mechanical behaviour of titanium alloy TiAl6V4 manufactured by selective laser melting: fatigue resistance and crack growth performance, Int. J. Fatigue 48 (2013) 300–307.

[44] B. Vayssette, N. Saintier, C. Brugger, M. El May, E. Pessard, Numerical modelling of surface roughness effect on the fatigue behavior of Ti-6Al-4V obtained by additive manufacturing, Int. J. Fatigue 123 (2019) 180–195.

[45] Z. Li, X. Jiang, H. Hopman, Surface crack growth in offshore metallic pipes under cyclic loads: a literature review, J. Mar. Sci. Eng. 8 (2020) 339.

[46] A. Frank, F.J. Arbeiter, I.J. Berger, P. Hutař, L. Náhlík, G. Pinter, Fracture mechanics lifetime prediction of polyethylene pipes, J. Pipeline Syst. Eng. Pract. 10 (2019) 1–14.